Structural Modeling of Compliance-Based Camber Morphing Structures under Transverse Shear Loading

Andres E. Rivero*, Paul M. Weaver†, Jonathan E. Cooper‡ and Benjamin K.S. Woods §
University of Bristol, Bristol, United Kingdom, BS8 1TR

A parametrically driven structural model based on Mindlin-Reissner plate theory is developed to capture the three-dimensional deflections of a compliance-based morphing trailing edge device with severe structural discontinuities. The model is used to study the Fish Bone Active Camber (FishBAC) device, which is represented as a discontinuous plate structure that captures the step changes in stiffness created by the concept's geometrical configuration. Courant's penalty method is implemented in the form of artificial penalty springs to account for stiffness discontinuities. A numerical validation is performed using Finite Element Analysis (FEA), followed by experimental validation under actuation loads. This analytical model represents a robust, efficient, mesh-independent and parameter-driven solution to modeling discontinuous plate structures. These traits make it useful for ongoing fluid-structure interaction analysis and optimisation of the FishBAC concept, and also for application to other complex composite structures.

I. Nomenclature

A_{ij}	=	Laminate's membrane stiffness matrix terms
a_i	=	Chordwise length in the x-direction
B_{ij}	=	Laminate's extension-bending coupling stiffness matrix terms
b_j	=	Spanwise length in the y-direction
D_{ij}	=	Laminate's bending stiffness matrix terms
E_{ij}	=	Young's Modulus in the i,j-direction
G_{ij}	=	Shear Modulus in the i,j-direction
ν_{ij}	=	Poisson's Ratio in the i,j-direction
H_{ij}	=	Transverse shear stiffness matrix terms
κ	=	Timoshenko shear correction factor

*Research Associate in Morphing Structures, Bristol Composites Institute, Department of Aerospace Engineering.
†Professor in Lightweight Structures, Bristol Composites Institute, Department of Aerospace Engineering.
‡RAEng Airbus Sir George White Professor of Aerospace Engineering, Department of Aerospace Engineering.
§Lecturer in Aerospace Structures, Bristol Composites Institute, Department of Aerospace Engineering.
Presented at the 2019 AIAA Scitech Forum,San Diego, California. 7-11 January 2019 (Manuscript No. AIAA 2019-0229)
Awarded the Harry H. and Lois C. Hilton Best Student Paper in Structures 2019. AIAA SciTech 2019 Forum, San Diego, CA

k_k = Artificial penalty spring stiffness

γ_{ij} = Transverse shear strain in the i,j-direction

Γ_x = Boundary conditions' circulation function

ϵ = Actuation mechanical efficiency factor

M_x = Applied distributed moments

ζ_i = Normalized chordwise position

η_j = Normalized spanwise position

$\overline{Q}_{ij}$ = Ply stiffness in the global coordinate system

u^o_{ij} = In-plane displacement in the chordwise x-direction

v^o_{ij} = In-plane displacement in the spanwise y-direction

w_{ij} = Out-of-plane displacement in the through-thickness z-direction

U = Strain energy

W = Potential energy due to external loads

ψ_x = xz-plane rotation

ψ_y = yz-plane rotation

$T(\zeta)$ = Chebyshev polynomials of the first kind

$X(x)$ = Chebyshev polynomial expansion in the x-direction

$Y(y)$ = Chebyshev polynomial expansion in the y-direction

ω = Servo actuator angular velocity

k_t = Torque Constant

II. Introduction

Morphing structures have been a subject of interest in the aerospace sector, in recent years, due to their ability to change shape without surface discontinuities. This characteristic makes them attractive for designing adaptive aircraft structures that can exploit this capability of changing shape to continuously optimize aerodynamic performance throughout flight [1]. Among all of the types of morphing techniques applicable to fixed-wing aircraft (e.g. span morphing, variable sweep, variable twist, etc.), camber morphing is the most commonly pursued. Aiming for smooth and continuous variations in airfoil camber, this technique represents a better alternative to varying camber using traditionally rigid and discontinuous hinged flaps—e.g. in ailerons, elevators, rudders, etc. Smooth changes in camber provide similar lift coefficient control authority with a much lower drag penalty [2]. Therefore, variable camber offers higher lift-to-drag ratios and lower noise than conventional control surfaces. Furthermore, unlike hinged flaps, camber morphing devices can be designed to vary their camber continuously along the span. This feature can potentially be used for controlling the spanwise lift distribution in real time, leading to induce drag reductions [3].

Another attractive aspect of camber morphing is that it can achieve large changes in aerodynamic forces and moments with relatively small changes in airfoil shape, which furthermore can be limited to the trailing edge of the

airfoil. This consideration makes camber morphing attractive in terms of maximising aerodynamic control authority while minimising the structural impact and actuation energy requirements [4].

Variable camber is not a new concept, indeed several camber morphing mechanisms were presented and patented in the 1920s and 1930s [5–7]. These concepts were not successfully implemented however, likely due in part to the use of heavy and complex mechanisms which made them unattractive for conventional applications. Due to advances in smart materials and structures in the last couple decades, there has been renewed interest in camber morphing, and many new concepts have been introduced. Specifically, research efforts have focused on smart material actuation, including using piezoelectric actuators [8, 9], shape memory alloys (SMAs) [3, 10], exploiting bistability in composite laminates [11, 12], developing zero-Poisson's Ratio cores [13], and also on shape optimization [14, 15].

One of the first "modern" morphing concepts was the NASA's F-111 Mission Adaptive Wing [16], which implemented sliding and bending skins over internal linkage mechanisms to achieve smooth leading and trailing edge camber deflections. Other highlighted concepts are the DARPA Smart Wing, where a combination of a plate structure with honeycomb and silicone skin is used [17]; the Flexys Flexfoil^{TM}, which can achieve a $\pm 10^{\circ}$ trailing edge deflection, as well as twist; the DLR Belt-Rib concept [18], and the Fish Bone Active Camber (FishBAC) device [19], which is the subject of study in this work.

The Fish Bone Active Camber (FishBAC) is a morphing trailing edge device capable of achieving large, smooth and continuous changes in camber without surface discontinuities (Fig. 1). It consists of a central bending plate (the spine) that defines the camber line and a series of spanwise stringers that support an elastomeric skin. The stringers are designed to provide a high level of spanwise rigidity without adding significant chordwise stiffness, while maintaining the airfoil's thickness distribution during morphing. The elastomeric skin is pre-tensioned before bonding to significantly increase out-of-plane stiffness (thereby reducing deformations under aerodynamic pressure loading) and to avoid skin buckling when in compression. The structure is actuated using antagonistic fabric tendons that transfer the actuation loads from a driving pulley to the trailing edge of the spine (Fig. 2). Current designs include two servo-based actuation points along the span, at equidistant points from the center of the wing. However, these are open design variables; the number and location of actuation points and type of actuators can be modified in accordance with design requirements, and the concept is "actuator agnostic" in that it can work with any type of actuator capable of generating rotational output.

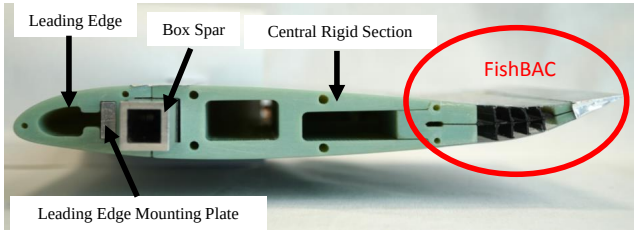

Fig. 1 Wind tunnel wing model with composite FishBAC trailing edge device

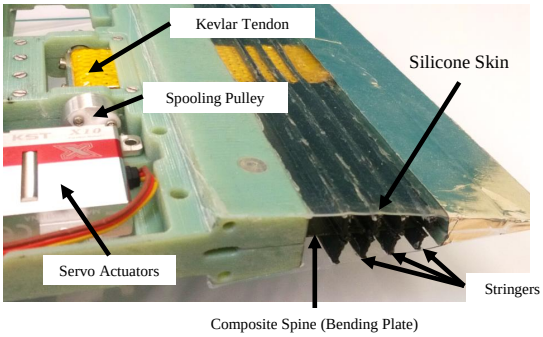

Fig. 2 FishBAC structure and actuation mechanism

Because of its geometrical configuration—a chordwise compliant spine with intermittent spanwise stringers and a compliant elastomer skin as the outer surface—the FishBAC is highly anisotropic: it is significantly more compliant in the chordwise direction than in the spanwise. This configuration allows obtaining large and continuous changes in camber with low actuation energy requirements, while providing significant spanwise rigidity. Furthermore, recent work has shown that using carbon fiber-reinforced polymer (CFRP) laminates in the FishBAC spine allows for further amplification of this anisotropic nature and adds another variable for tailoring structural stiffness [20].

To analyze and design carbon fiber FishBAC devices, a two-dimensional structural model capable of analyzing composites laminates is needed. Therefore, a Kirchhoff-Love based plate theory model was developed in previous work by the authors [21] to analytically study the static behavior of a composite FishBAC under transverse pressure and actuation loads. Although successful in predicting deflections under uniform transverse pressure and uniform actuation loads (when validated against Finite Element Analysis), the model failed to accurately predict deflections when the FishBAC is subject to spanwise twist due to asymmetric actuation loads. The authors showed that this limitation is caused by the existence of transverse shear strains due to torsion, which cannot be captured using Kirchhoff-Love plate theory because it neglects transverse shear strains.

The objective of this work is to address these limitations and enhance the modeling technique proposed by Rivero et al. [21]. This goal is achieved here by replacing the Kirchhoff-Love plate model with Mindlin-Reissner plate theory [22], which models transverse shear deformations by applying a First-Order Shear Deformation Theory (FSDT), which assumes that transverse shear displacements vary linearly across the thickness of the structure [23]. This enhanced analytical structural model, implemented in MATLAB® R2016a, is validated both numerically and experimentally. The numerical validation was performed using Finite Element Analysis (FEA), developed in ABAQUS/CAE® 6.14-1, whereas the experimental validation was performed using a composite FishBAC wing prototype developed for wind tunnel testing [24].

The novelty of this work resides in the ability of this model to capture displacements of a highly discontinuous plate structure subjected to different load cases—including transverse shear loads—using a series of individual plates

that are joined together using artificial penalty springs. This model will become a key element in future design, optimization and fluid-structure interaction analysis of the FishBAC. Moreover, its use is not exclusive to the FishBAC device; any geometrically linear continuous or discontinuous composite plate-type structure can be modeled with this technique. This article will first introduce the modeling technique, including the solution method, boundary conditions and assumptions. It then describes the Finite Element Analysis used for validation purposes, followed by a static experimental validation using the composite-spine wind tunnel wing model.

III. Analytical Structural Model

The analytical structural model that is developed in this article is based on the Rayleigh-Ritz Method, which is used to solve the plate differential equation using a weak formulation. Furthermore, Classical Laminate Theory (CLT) extended for Mindlin-Reissner plates is used to calculate the stiffness terms [25]. This solution technique requires the use of assumed shape functions, in this case, the authors have selected Chebyshev Polynomials of the First Kind. Lastly, to account for the large number of chordwise and spanwise stiffness discontinuities created by the stringers and discrete actuation inputs, the structure is discretized in sections of uniform stiffness that are joined using the Courant's penalty method in the form of artificial springs [26]. This approach is similar to the Equivalent Plate Theory used by several authors to model and optimize tapered wings [27–30]. However, the main difference is that the equivalent plate theory does not account for stiffness variations along the chord, which limits its use to model spanwise changes in geometry (e.g. taper).

A. Mindlin-Reissner Plate Theory

In beam analysis, Euler-Bernoulli beam theory is unable to accurately predict deflections of thick beams. This limitation is due to its inability to represent transverse shear deformations. In response to this, Timoshenko developed his famous transverse shear deformation theory of beams [31]. Similarly, Kirchhoff-Love plate theory is analogous to Euler-Bernoulli beam theory and is likewise unable to model the behavior of thick plates as it assumes no through-thickness shear deformations. Mindlin-Reissner Plate Theory extends Kirchhoff-Love Plate Theory to include the effects of transverse shear deformations by allowing the rotation of the through-thickness normal planes. It assumes that transverse shear displacements vary linearly across the thickness of the plate, thus, it is also known as the First-Order Shear Deformation Theory of Plates (FSDT) [32].

In order to solve the Mindlin-Reissner equations with the Rayleigh-Ritz Method, a strain energy formulation of the plate's differential equation is needed. This equation considers total strain energy in the plates as the summation of strain energies due to stretching and bending and transverse shear [25, 33]

$$
\begin{aligned}
U_{ABD} = \frac{1}{2}\iint & A_{11}\left(\frac{\partial u^o}{\partial x}\right)^2 + 2A_{12}\frac{\partial u^o}{\partial x}\frac{\partial v^o}{\partial y} + A_{22}\left(\frac{\partial v^o}{\partial y}\right)^2 + 2\left(A_{16}\frac{\partial u^o}{\partial x} + A_{26}\frac{\partial v^o}{\partial y}\right)\left(\frac{\partial u^o}{\partial y} + \frac{\partial v^o}{\partial x}\right) + A_{66}\left(\frac{\partial u^o}{\partial y} + \frac{\partial v^o}{\partial x}\right)^2 \\
& - 2B_{11}\frac{\partial u^o}{\partial x}\frac{\partial \psi_x}{\partial x} - 2B_{22}\frac{\partial v^o}{\partial y}\frac{\partial \psi_y}{\partial y} - 2B_{12}\left(\frac{\partial v^o}{\partial y}\frac{\partial \psi_x}{\partial x} + \frac{\partial u^o}{\partial x}\frac{\partial \psi_y}{\partial y}\right) - 2B_{66}\left(\frac{\partial u^o}{\partial y} + \frac{\partial v^o}{\partial x}\right)\left(\frac{\partial \psi_x}{\partial y} + \frac{\partial \psi_y}{\partial x}\right) \\
& - 2B_{16}\left[\frac{\partial \psi_x}{\partial x}\left(\frac{\partial u^o}{\partial y} + \frac{\partial v^o}{\partial x}\right) + \frac{\partial u^o}{\partial x}\left(\frac{\partial \psi_x}{\partial y} + \frac{\partial \psi_y}{\partial x}\right)\right] - 2B_{26}\left[\frac{\partial \psi_y}{\partial y}\left(\frac{\partial u^o}{\partial y} + \frac{\partial v^o}{\partial x}\right) + \frac{\partial v^o}{\partial y}\left(\frac{\partial \psi_x}{\partial y} + \frac{\partial \psi_y}{\partial x}\right)\right] + D_{11}\left(\frac{\partial \psi_x}{\partial x}\right)^2 \\
& + D_{22}\left(\frac{\partial \psi_y}{\partial y}\right)^2 + D_{66}\left(\frac{\partial \psi_x}{\partial y} + \frac{\partial \psi_y}{\partial x}\right)^2 + 2D_{12}\left(\frac{\partial \psi_x}{\partial x}\frac{\partial \psi_y}{\partial y}\right) + 2D_{16}\frac{\partial \psi_x}{\partial x}\left(\frac{\partial \psi_x}{\partial y} + \frac{\partial \psi_y}{\partial x}\right) + 2D_{26}\frac{\partial \psi_y}{\partial y}\left(\frac{\partial \psi_x}{\partial y} + \frac{\partial \psi_y}{\partial x}\right) dx\, dy \quad (1)
\end{aligned}
$$

$$
U_H = \frac{1}{2}\iint \left[H_{44}\left(\frac{\partial w}{\partial y} - \psi_y\right)^2 + 2H_{45}\left(\frac{\partial w}{\partial y} - \psi_y\right)\left(\frac{\partial w}{\partial x} - \psi_x\right) + H_{55}\left(\frac{\partial w}{\partial x} - \psi_x\right)^2\right] dx\, dy, \quad (2)
$$

where A_{ij}, B_{ij},D_{ij} and H_{ij} matrices are the plate's material and geometric stiffness, u^o, $v^o$and w are the plate displacements and ψ_x and ψ_y are the plate rotations. Note the subscript ABD in Eq. (1) denotes the strain energy terms present in Kirchhoff-Love theory, whereas the subscript H in Eq. (2) denotes the additional terms added by Mindlin-Reissner theory to capture the strain energy due to transverse shear. These plate rotations include transverse shear strains, such that

$$
\psi_x = \frac{\partial w}{\partial x} - \gamma_{xz} \qquad \text{and} \qquad \psi_y = \frac{\partial w}{\partial y} - \gamma_{yz} \quad . \quad (3)
$$

The A_{ij},B_{ij} and D_{ij} terms in Eq. (1)— commonly known as the ABD matrix—are, respectively, the extension, bending-coupling and bending material and geometric stiffness of the laminate, and these are obtained using Classical Laminate Theory (CLT) [34]. Furthermore, the H_{ij} terms in Eq. (2) correspond to the transverse shear stiffness, and are derived from the expression

$$
H_{ij} = \frac{1}{\kappa}\int_h \overline{Q}_{ij}\, dz = \frac{1}{\kappa}\sum_{k=1}^{K} \overline{Q}_{ij,k}(z_k - z_{k-1})\, dz\,, \quad (4)
$$

where $i, j = 4, 5$ and κ is known as the Timoshenko Shear Correction Factor, which has an approximate value of $6/5$ for rectangular cross-sections. Although this approximation is valid for isotropic plates, it has been shown to provide accurate results when used to model composite laminates [33]. Therefore, a value of $\kappa = 6/5$ is used throughout this study. Lastly, the $\overline{Q}_{ij}$ terms correspond to the stiffness of each ply in the global coordinate frame, which are a function of fiber orientation angle and the following material properties: E_{11}, E_{22}, ν_{12}, G_{12}, G_{13} and G_{23}, in which the subscripts $i, j = 1, 2, 3$ refer to the fiber, transverse and trough-thickness directions, respectively.

B. Shape Functions and Boundary Conditions

When solving the plate equation by minimizing total energy (i.e. by using Rayleigh-Ritz Method), the displacements and transverse shear strains of the plate are unknown—and become the independent variables of the problem. Therefore, the underlying shape functions of the displacements and transverse shear strains need to be assumed, such that the corresponding amplitudes can be solved for. Commonly, when in 2-D, these are assumed in the form of a double summation in x and y. Therefore, the three displacements become

$$u^0_{ij} = \sum_{m=0}^{M}\sum_{n=0}^{N} O^{ij}_{mn} X^i_m(x) Y^j_n(y) \ , \quad v^0_{ij} = \sum_{m=0}^{M}\sum_{n=0}^{N} P^{ij}_{mn} X^i_m(x) Y^j_n(y) \quad \text{and} \quad w_{ij} = \sum_{m=0}^{M}\sum_{n=0}^{N} R^{ij}_{mn} X^i_m(x) Y^j_n(y) \ , \tag{5}$$

and the transverse plane rotations have a similar form

$$\psi_x = \sum_{m=0}^{M}\sum_{n=0}^{N} S^{ij}_{mn} X^i_m(x) Y^j_n(y) \quad \text{and} \quad \psi_y = \sum_{m=0}^{M}\sum_{n=0}^{N} V^{ij}_{mn} X^i_m(x) Y^j_n(y) \ . \tag{6}$$

In this study, orthogonal polynomials are chosen as the assumed shape functions because, unlike simpler formulations, they can successfully predict deflections when a high degree of anisotropy exists. Specifically, the type of orthogonal polynomials that are implemented are the Chebyshev Polynomials of the First Kind. This selection is motivated by Rivero et al. [21], where the authors explain that Chebyshev Polynomials of the First Kind allow for direct integration in a normalized domain without leading to values of zero. For additional details on how these polynomials are integrated and coordinate frames are normalized, please refer to Rivero et al. [21].

Lastly, it is important to implement the correct boundary conditions. In this particular application, the FishBAC is modeled as a cantilever plate that is clamped at one of its chordwise edges. It can be observed in Fig. 3 that Chebyshev Polynomials do not naturally meet this condition, as they have non-zero displacements at the boundaries. Therefore, the clamped condition needs to be enforced separately. To achieve this, a circulation function [35]

$$\Gamma_x(\zeta) = (\zeta - \zeta_c)^n \ , \tag{7}$$

is added as a multiplier to the displacement and rotations (i.e. Eqs. (5-6)). This condition forces certain boundary condition at a location ζ_c and the type of boundary condition is set by choosing the value of n. The relevant values for different conditions are given in depth in Table 1. Furthermore, it is important to note that using this circulation function does not affect the orthogonality of the Chebyshev Polynomials—so as long as every polynomial term in the expansion is multiplied by it.

As the FishBAC structure is modeled as a clamped plate, all three translations $u^o, v^o$and w and two rotations ψ_x, ψ_y must be equal to zero at the root. However, the transverse shear strains γ_{xz}, γ_{yz} need not be zero, as transverse shear straining at the root is a likely deformation mode [36]. Hence, for a clamped edge, a value of $n = 1$ must be used in Eq. (7), as this yields zero displacement and rotations at the root, while still allowing for non-zero transverse shear strains at this location.

The derivatives of the Chebyshev Polynomials that are required to solve Eq. (1) are computed analytically, while all of the required integrations in this analytical model are computed numerically using MATLAB's adaptive quadrature functions 'integral' and 'integral2', for 1-dimensional and 2-dimensional integrals, respectively. Because all integrals are computed in a normalized coordinate system, these can be calculated beforehand and their values can be stored and then transformed to the physical coordinate system, as long as the relationship between the normalized and physical coordinate systems is assumed to be constant (i.e. constant Jacobian with rectangular elements). This property leads to a significant reduction of the computational cost of running this analytical model as the integrals have to be performed only once "up front" for each set of boundary conditions. This development represents a significant improvement over the previous approach from Rivero et al. [21], which required "on line" calculation of these integrals.

However, one disadvantage of this modeling approach is that the use of orthogonal polynomials in high aspect ratio rectangular

Table 1 Boundary Conditions as implemented by circulation function in Equation (7) [33, 36]

Boundary Condition at ζ_c	$n_{\text{displacement}}$	n_{rotation}	Disp. (u^o, v^o, w)	Rot. (ψ_x, ψ_y)	Transverse Shear Strains $(\gamma_{xz}, \gamma_{yz})$
Free Edge (F)	0	0	Free	Free	Free
Simply Supported (SS)	1	0	0	Free	Free
Clamped (C)	1	1	0	0	Free

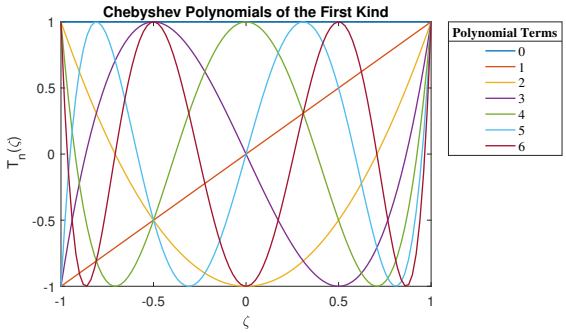

Fig. 3 Chebyshev Polynomials of the First Kind in a normalized domain

elements may lead to ill-conditioning. These numerical instabilities are attributed to rounding errors when high-order terms (and their derivatives) are integrated. To mitigate ill-conditioning, Ilanko et al. (2015) recommend selecting the minimum possible number of orthogonal polynomial functions with the lowest possible order, while still ensuring convergence [26].

C. Stiffness Discontinuities

Due to the presence of stringers, the chordwise taper of the airfoil thickness, and the presence of localized actuation sections along the span, the stiffness of the FishBAC structure is discontinuous. To account for this, the FishBAC is modeled in this work as individual plate units of uniform stiffness that are joined together using a series of artificial penalty springs. These penalty springs act by enforcing displacement and rotation continuity at the joints of each partition, so as long as the artificial penalty springs is 'large' enough (i.e. usually between 10^6 and 10^{12} $\mathrm{N\,m^{-1}}$) [37]. Although different penalty spring stiffness k_k at each joint can be specified, it was decided to use the same value for all penalty springs for simplicity reasons.

To implement this approach within the Rayleigh-Ritz Method, the strain energy of these artificial springs need to be minimized to enforce displacement and rotation compatibility at joints. The penalty spring energy due to displacements is derived by Rivero et al. (2018) [21]. Also, the rotation penalty terms are defined as

$$U_{prx,kl} = \frac{k_k}{2}\int_{-b_j/2}^{b_j/2}(\psi_{x_k}(x_{kl}^{(+)}, y_j) - \psi_{x_l}(x_{kl}^{(-)}, y_j))^2 dy \quad \text{and} \quad U_{pry,kl} = \frac{k_k}{2}\int_{-b_j/2}^{b_j/2}(\psi_{y_k}(x_{kl}^{(+)}, y_j) - \psi_{y_l}(x_{kl}^{(-)}, y_j))^2 dy \ . \tag{8}$$

For more details on how the penalty method is applied in this model, please refer to Rivero et al. (2018) [21].

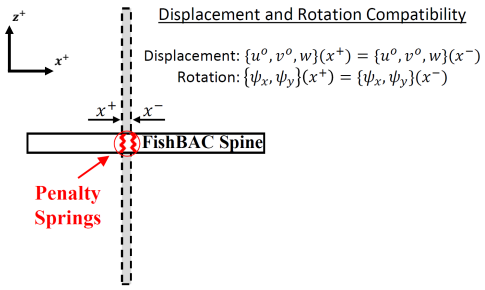

Fig. 4 Displacement and rotation compatibility enforced at each plate-stringer joint using artificial penalty springs.

D. Actuation Loads

As previously mentioned, the composite FishBAC prototype is actuated at two locations along the span of the wing which are equidistant from the center. This actuation is currently performed by a set of two servo actuators, at each actuation point, that drive a tendon spooling pulley. This pulley is connected to a Kevlar tendon tape that travels through slots in the stringers until reaching the trailing edge portion of the composite spine—where it is stitched and bonded directly to the spine. In this way, torque and rotation input to the spooling pulley is transformed into force and displacement of the tendons, before being transformed back into a bending moment at the trailing edge. It is this bending moment which drives the morphing deformation. To capture the impact of this actuation method within this analysis, the external actuation loads are incorporated as an additional source of potential energy. These are modeled as applied distributed moments over each short actuated segment of the FishBAC, according to the expression

$$W_{ij} = -\int M_x \, \psi_x(a_i, y) \, dy \ , \tag{9}$$

where a_i is the location where the distributed moment is applied. Note that this neglects any friction on the pulley-tendon system.

E. Rayleigh-Ritz Method: Minimum Potential Energy

As mentioned in the introduction, the solution method that this structural model is based upon is the principle of conservation of energy. In this structural model, there are no non-conservative energy losses (such as friction), and so the total energy of the system is constant. Any frictional losses in the experimental results are later accounted by estimating the actuation efficiency factor, as later explained in Section VI.A.

Therefore, if the total energy is defined as the sum of strain energy and potential energy due to external loads

$$\Pi(u^0, v^0, w, \psi_x, \psi_y) = U_{ABD} + U_H + U_{penalty} + W = \text{constant} \quad , \tag{10}$$

differentiation with respect to the unknown amplitudes O^{ij}_{mn}, P^{ij}_{mn}, R^{ij}_{mn}, S^{ij}_{mn} and V^{ij}_{mn} leads to a state of minimum potential energy—where the right hand side of Eq. (10) is equal to zero [38]. This feature allows a system of $5 \times (M \times N) \times (i \times j)$ independent linear equations to be generated, such that

$$\frac{\partial \Pi}{\partial O_{mn}^{ij}}, \frac{\partial \Pi}{\partial P_{mn}^{ij}}, \frac{\partial \Pi}{\partial R_{mn}^{ij}}, \frac{\partial \Pi}{\partial S_{mn}^{ij}}, \frac{\partial \Pi}{\partial V_{mn}^{ij}} = 0 \quad \begin{cases} m = 1, 2, ..., M \\ n = 1, 2, ..., N \end{cases} . \tag{11}$$

This analytical model represents a fast approach to modeling the behavior of the FishBAC morphing device using 1% of degrees of freedom (DOFs), compared to Finite Element Analysis. Due to the multi-plate assembly procedure and its mesh-independence, this model allows for simple, fast, parameter driven analysis of new FishBAC configurations. The authors have used this approach to automate the generation of completely different FishBAC geometries from simple vectorized inputs of geometry and material properties. This allows for easy modification of the dimensions, airfoil, detailed component geometries, material properties, and stacking sequence. Note that these changes in parameters do not significantly impact the convergence of the model.

IV. FishBAC Morphing Wing: Material Properties and Dimensions

This section introduces the characteristics of a composite FishBAC wind tunnel wing model, which is the structure that is modeled in this study. The main structure corresponds to the first ever composite-spine carbon fiber FishBAC, which has been designed and manufactured for wind tunnel testing. The wind tunnel wing model is a rectangular planform NACA 23012 wing with a chord of 270 mm and a span of 1000 mm, with the FishBAC occupying the aft 69 mm of the chord. It has two actuation points with tendons mounted 415 mm in either direction from the center of the wing span: one on the left hand side (M_{x_2}) and one on the right hand side (M_{x_4}), when viewed from above. Fig. 5 shows a schematic diagram of this structural configuration and its primary dimensions.

A. Wind Tunnel Wing Model

The wind tunnel wing model was designed and manufactured using a combination of metallic and 3D-printed plastic parts, with silicone sheet skins and a carbon fiber spine. The spine was manufactured using Hexcel®'s 8552/IM7 carbon fiber prepreg under vacuum bag and autoclave pressure curing. With a total cured ply thickness of 0.39 mm, this composite FishBAC provides another level of anisotropy—beyond what the plate-stringer configuration provides—as it has a layup ($[90/0/90]_T$), which produces low chordwise bending stiffness to minimise actuation requirements while maintaining spanwise stiffness to reduce elastic washout.

A series of 3D-printed plastic (Digital ABS Plus by Stratasys) stringers and trailing edge sections were bonded to the cured composite spine using Cyanoacrylate adhesive. Whereas the use of plastic for the stringers implies that the spanwise bending stiffness of this FishBAC is significantly lower than a fully composite version, the choice was made to use 3D printed polymer to reduce the complexity and risk of this first attempt at a composite FishBAC. This feature significantly increases the amount of elastic washout of

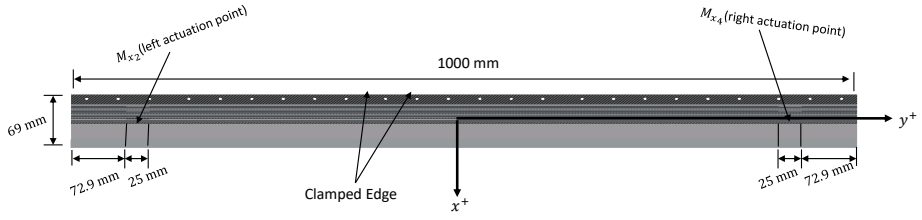

Fig. 5 FishBAC wind tunnel wing model global dimensions and actuation points

deformation which occurs along the span (particularly for more highly loaded cases), but can be readily addressed in future designs. The structure is actuated at two locations using a total of four KST X10 HV servo actuators—two in each location [39]. As mentioned above, the actuation loads are transferred to the spine by a pulley-tendon system using a Kevlar-tape tendon that is stitched to the carbon plate. Finally, a pre-tensioned elastomeric silicone sheet covers the FishBAC structure and provides the airfoil shape. Fig. 6 shows a close-up view of the composite FishBAC morphing device—note that the fairing that covers the very rear of the trailing edge were removed for this photograph.

B. Material Characterization

In order to predict the deflections of the FishBAC, a material characterisation was performed to obtain experimental stiffness and Poisson's ratio values. The carbon fiber used for this material characterisation was cured in the same vacuum bag as the FishBAC spine and underwent the same curing cycle.

The carbon fiber's 0° and 90° Young's modulus are determined in accordance with ASTM D3039 test standard [40], whereas the in-plane shear modulus is determined using ASTM D3518's test standard [41]. Furthermore, the ABS 3D-printed plastic was tested by following ASTM D638's test standard guidelines [42]. Finally, the silicone skin was tested using 25 mm × 150 mm samples, which where bonded to 3D-printed ABS end tabs to not only test the Young's modulus of the silicone skin, but also to test the adhesive that was used to bond the skin on the FishBAC wing. Tables 2 and 3 present the results of these material tests, which are the material properties that are used in both analytical and FEA models.

Fig. 6 Composite FishBAC device used for experimental validation of the analytical structural model

Table 2 Material properties of the 8552/IM7 carbon fiber prepreg. Properties obtained via tensile tests.

Material	E_{11} [GPa]	E_{22} [GPa]	G_{12} [GPa]	ν_{12}
8552/IM7 Carbon fiber	169.50	8.58	5.03	0.28

Table 3 Material properties of Isotropic silicone and ABS plastic. Properties obtained via tensile tests.

Material	E [MPa]	G [MPa]	ν
40° Shore Silicone	1.18	0.427	0.39
ABS Plastic	2010	728	0.38

V. Numerical Validation: Finite Element Analysis

In order to provide a reference for validation and comparison, a Finite Element Analysis (FEA) model of the FishBAC was created in Abaqus/CAE 6.14 using a combination of shell and solid elements (Fig. 7). The composite plate, stringers and skin are modeled using four-node shell elements (S4R), whereas the thick non-morphing sections of the FishBAC are modeled using solid eight-node elements (C3D8R). In terms of material definitions, the spine is modeled as a composite laminate—on a ply-by-ply basis—and the stringers, solid trailing edge sections and skin are modeled as isotropic regions. The solid and shell elements are connected using the *Shell-to-Solid* constraint in ABAQUS/CAE, which couples the motion of solid and shell nodes at the shell-to-solid boundary.

A fully clamped boundary condition is applied at the root of the FishBAC and the actuation loads are introduced as distributed moments at the tendon-spine anchor points. To transfer these actuation loads to the solid elements, two external reference points are created and coupled via *Kinematic Coupling* to the node sets that correspond to the anchor points. This coupling transfers rotation from the point moments to the solid elements. Furthermore, displacements are tracked along all three free edges of the FishBAC at the nodes located at the center of the spine (in the through-thickness direction), and are then used to validate the analytical model. Finally, the FishBAC's skin pre-tensioning is modeled by applying a pre-defined stress field equal to the Young's modulus of the silicone times a strain of $\epsilon_x = 0.3$, which corresponds to the applied 30% pre-tension of the skin in the wing tunnel wing model.

A comparison between linear and nonlinear analysis was performed and it was determined that the difference between both approaches was negligible, suggesting that the FishBAC behaves linearly, in the geometric sense, for the range of deflections that are considered in this study. Therefore a linear FEM analysis was performed throughout. Finally, a mesh-convergence study was performed by tracking tip displacements when the overall element size was reduced from 10 mm to 2.5 mm (in increments of 2.5 mm). The mesh was considered to be converged when both tip displacements varied by less than 0.5%, with respect to the previous meshing iteration. A nominal element size of 5 mm was used to mesh the structure, resulting on a total of 231 167 elements.

The comparison between the discontinuous Mindlin-Reissner and the FEM models is performed in terms of the percentage error difference along the spanwise free edge. Besides obtaining displacement fields under several load cases, two convergence studies were performed: the first one to estimate the required number of polynomial terms to achieve convergence and the second one to determine the stiffness of the artificial penalty springs. The stacking sequence and geometrical dimensions used correspond to the manufactured FishBAC wind tunnel wing model (i.e. stacking sequence of $[90^\circ/0^\circ/90^\circ]_T$ and spine thickness of $t = 0.39$ mm).

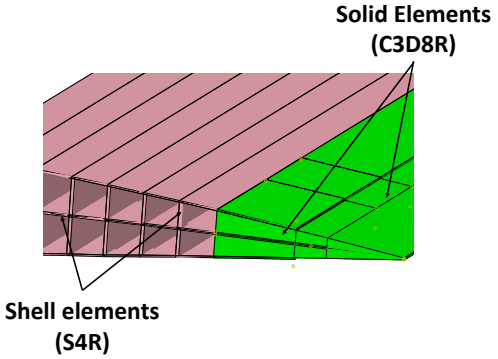

Fig. 7 A combination of shell and solid elements are used to model the complex FishBAC structure in Abaqus/CAE FEA software.

The FishBAC structure is discretized into 16 chordwise and 5 spanwise partitions of uniform thickness. These 16 chordwise partitions capture the presence of the stringers and the geometric taper of the airfoil. The tapered trailing edge is modeled as 7 sections of constant average height. While the trailing edge could be discretized into more partitions, this region of the airfoil is relatively rigid and adding partitions increases the size of the system of equations (Eq. (11)), and so 7 partitions was found to be sufficient.

A. Analytical Model: Polynomial Term Convergence

A convergence study was performed to determine the number of Chebyshev Polynomial terms needed to capture the deformed shapes with sufficient accuracy while avoiding unnecessary computational cost. In this study, the same FishBAC geometrical configuration was used and, for simplicity purposes, the number of chordwise and spanwise terms in each plate segment are equal to each other (although more plate segments are used along the chord than along the span). To assess convergence, both maximum and root-mean-square (RMS) percentage errors are calculated along the free spanwise edge. The chosen load case for this convergence study is a differential moment input of $M_{x_2} = -1\,\mathrm{N\,m}$ and $M_{x_4} = 1\,\mathrm{N\,m}$, respectively. This corresponds to the load case that the Kirchhoff-Love formulation was unable to model, while the selected moment magnitudes yield to deflections that are similar to the maximum ones that can be achieved by the composite wind tunnel prototype.

Table 4 shows a summary of the corresponding percentage errors, and Fig. 8 also shows the stability of the system of equations—in terms of the condition number[1] —and the total computational time per iteration. It is important to note that all results were computed on a single Intel® Core™ i7-4790 3.60 GHz CPU processor, using a 64-bit OS with 32 GB of physical memory. Results show convergence with as few as three polynomial terms (in each direction), with a 4.2% and 2.7% maximum and RMS percentage errors, respectively. It can also be observed that increasing the number of terms only reduces both errors by a maximum of $\approx 1\%$. Furthermore, results show that the maximum error has a minimum value at five polynomial terms, and then increases with additional terms. This is due to the increase in condition number of the coefficient matrix when the number of polynomial terms is increased, as the system becomes more sensitive to small changes in input. It can be concluded from this convergence study that this model, converges at five Chebyshev Polynomial terms, for this combination of material and geometrical properties.

Table 4 Comparison of Analytical and geometrically linear FEA results as a function of Chebyshev Polynomials terms (polynomial order).

Laminate	Material	Polynomial Terms (M=N)	Max. Error (Abs. Value) [%]	RMS Error [%]	DOF
$[90°/0°/90°]_T$	8552/IM7 Carbon fiber	2	99.90	43.00	1600
		3	4.172	2.688	3600
		4	3.478	1.879	6400
		5	3.287	1.686	10000
		6	5.740	1.645	14400
		7	5.728	1.618	19600
		8	5.097	1.465	25600

[1]The condition number of a matrix is defined as the product of the Euclidean norm of the matrix and its inverse, such that $\kappa(A) = \|A\|\|A^{-1}\|$. A high condition number indicates an 'ill-conditioned' system, which are more sensitive to changes in response due to small changes in input [43, 44].

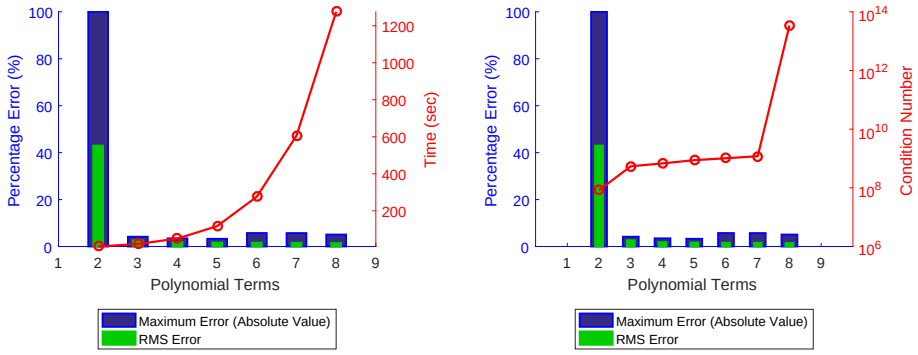

Fig. 8 Convergence study of analytical Mindlin-Reissner plate model versus Finite Element Analysis. Study also analyzed the stability of the system—in terms of the condition number—and the total computation time of each iteration. A spring stiffness of $k = 10^7$ N m^{-1} was used for this convergence study.

B. Penalty Stiffness Convergence

A second convergence study was performed to determine the impact that the artificial penalty spring stiffness values have on the stability of the solution. The objective of this convergence study is to determine whether the discontinuous Mindlin-Reissner model converges for spring stiffness values between 10^6 N m^{-1} and 10^{12} N m^{-1}—as similar models in the literature do [23, 37]. To assess this, the spanwise RMS error and the condition number are calculated for different penalty stiffness values. Fig. 9 shows the results of this convergence study, where it can be observed that the solution remains stable in terms of percentage error for penalty spring stiffnesses between $k = 10^6$ N m^{-1} and $k = 10^{13}$ N m^{-1}. This is consistent with other structural models that implement this technique [21, 33, 37]. Furthermore, a minimum percentage error is observed when the penalty stiffness is $k = 10^6$ N m^{-1}, however, this value may vary depending on the geometric and material configuration, as well as the number of polynomial terms. Consequently, it is considered that a value of $k = 10^7$ N m^{-1} guarantees convergence throughout this study, as it presents a stable condition number and low percentage error. Therefore, a value of $k = 10^7$ N m^{-1} is used during the rest of this study.

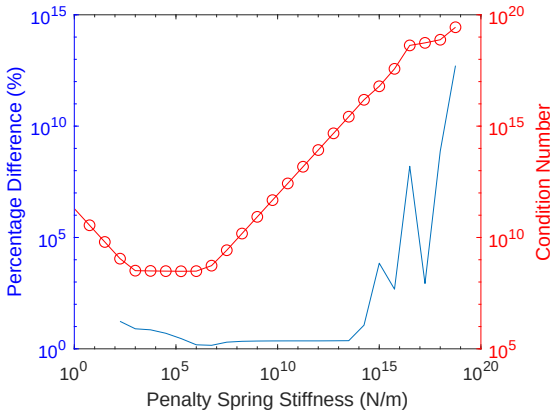

Fig. 9 Root-mean-square error—along the spanwise edge—and condition number, as a function of penalty spring stiffness. Note that, for values lower than $k = 10^2$, there is no solution as the coefficient matrix is singular.

C. Kirchhoff-Love vs. Mindlin-Reissner Model

The presented discontinuous Mindlin-Reissner model was primarily developed to address the inability of a discontinuous Kirchhoff-Love plate theory to capture deflections when differential actuation loads are applied (i.e. actuation moment loads with opposite direction). It was determined that this inability was due to the presence of transverse shear, as the structure reacts this load case by twisting, which induces transverse shear on the yz-plane. Since Kirchhoff-Love models cannot capture transverse shear deformations, a First-Order Transverse Shear Deformation (FTSD) approach was implemented. Fig. 10 shows a direct comparison between Kirchhoff-Love, Mindlin-Reissner and FEA models, when the FishBAC is loaded under differential actuation (i.e. equal magnitude but opposite direction). On the one hand, it can be observed that the Kirchhoff-Love model fails to predict the FishBAC displacement (compared to FEA), presenting a RMS percentage error —along the spanwise edge— of 35 %. On the other hand, it can be observed that the Mindlin-Reissner model successfully captures the displacement of the FishBAC, presenting an RMS percentage error of less than 2%. This result highlights the importance of developing this new model, which will be used for further design, optimization and fluid-structure interaction modeling of this morphing concept.

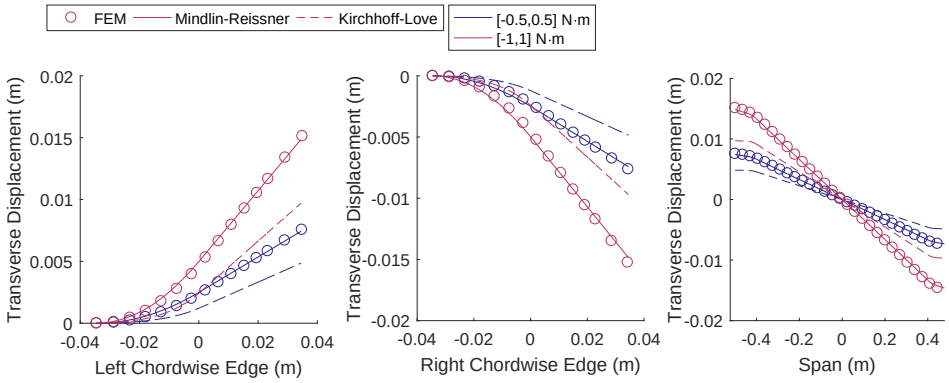

Fig. 10 Comparison between Kirchhoff-Love (dash) and Mindlin-Reissner (solid) discontinuous plate models and Finite Element Analysis (circle).

D. Comparison Study: Mindlin-Reissner vs. FEA

A more thorough comparison study of FEA vs. analytical displacement fields was also performed. Three different load cases were considered: uniform actuation (i.e. equal magnitude and direction), differential actuation (i.e. equal magnitude, but opposite direction) and single input (i.e. only one actuation input instead of two). The following subsection presents these results.

1. Uniform Actuation

The uniform actuation case corresponds to equal actuation inputs—in magnitude and direction—at both FishBAC's actuation points. Figs. 11 and 12 show a comparison between analytical and FEA results, showing an agreement with a maximum and RMS percentage error—along the spanwise edge—of 12.94% and 7.485%, respectively. One important characteristic of these displacement fields is the significant elastic washout along the span, which both models are able to capture. As mentioned above, this is due to the

use of plastic instead of carbon fiber composite for the stringers in the wind tunnel wing model. While future designs will most likely be stiffer in the spanwise direction, the ability to capture the washout created by spanwise compliance is still crucial to the efficacy of this model, as washout will significantly impact the aerodynamic performance.

2. *Single Actuation Input*

This load case corresponds to having actuation input to only one actuation point. To simulate this case, negative actuation inputs between $M_{x_4} = -0.25\,\mathrm{N}\cdot\mathrm{m}$ and $M_{x_4} = -1\,\mathrm{N}\cdot\mathrm{m}$ were applied at the right-end actuation point, while the left-end actuation input was set to zero. Fig. 13 shows these results, which present a maximum and RMS error—along the spanwise edge—of 13.70% and 9.132%, respectively. This actuation case is primarily reacted as bending on the chordwise direction, with significant displacement variations along the span. This type of actuation case could potentially be useful for controlling spanwise aerodynamic loads, as different lift distributions along the span can be obtained.

3. *Differential Actuation*

The differential actuation case consists of applying torque inputs of equal magnitude but opposite sign to the two actuation points. In addition to chordwise bending moments, this creates a net torque on the FishBAC structure, inducing transverse shear. Consequently, this scenario cannot be accurately captured using Kirchhoff-Love Plate Theory.

Actuation inputs of magnitudes between $M_x = 0.25\,\mathrm{N\,m}$ and $M_x = 1\,\mathrm{N\,m}$, in increments of $0.25\,\mathrm{N\,m}$, are applied. Fig. 14 shows the displacement fields obtained using both FEA and the analytical model. It can be observed that the FEA and analytical results agree with each other (Fig. 14), with a maximum and RMS percentage error—along the free spanwise edge—of 3.28% and 2%, respectively. This is a significant improvement from the Kirchhoff-Love model, which presents a RMS percentage error of 33%.

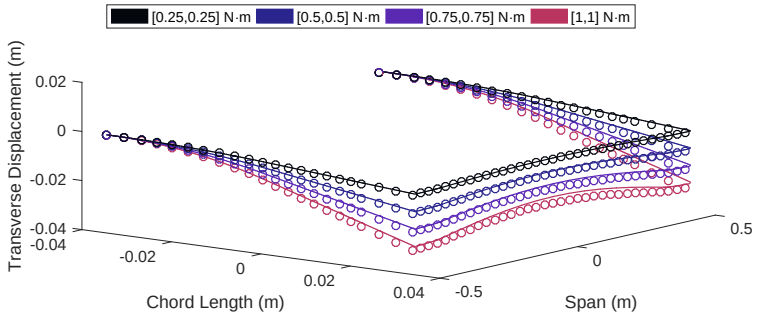

Fig. 11 Mindlin-Reissner discontinuous plate model vs. FEA under uniform actuation loads (trailing edge down). Solid lines correspond to analytical result, whereas circle markers to FEA.

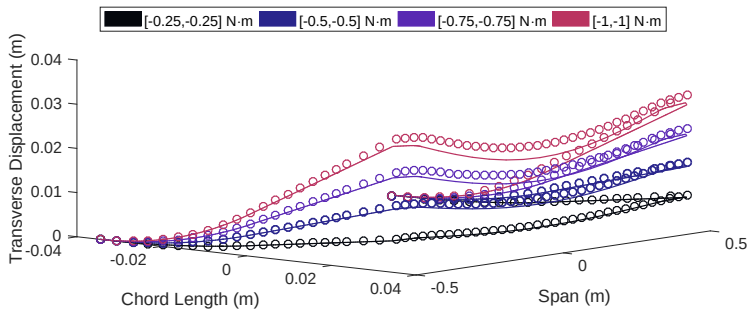

Fig. 12 Mindlin-Reissner discontinuous plate model vs. FEA under uniform actuation loads (trailing edge up). Solid lines correspond to analytical result, whereas circle markers to FEA.

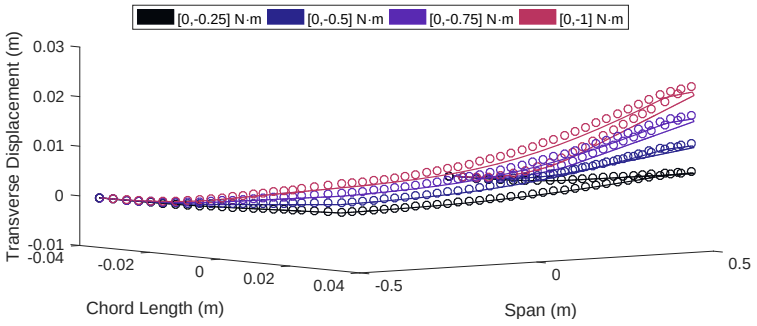

Fig. 13 Mindlin-Reissner discontinuous plate model vs. FEA under a single actuation load. Solid lines correspond to analytical result, whereas circle markers to FEA.

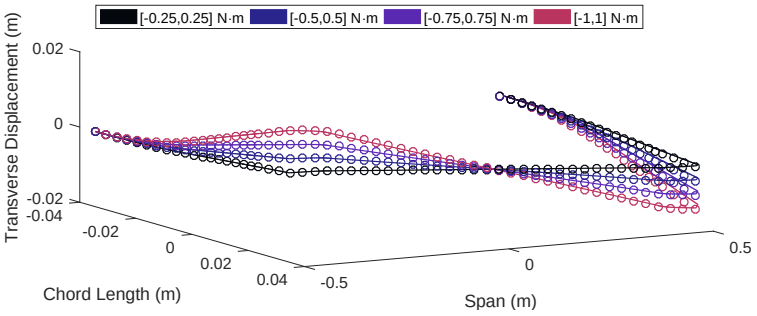

Fig. 14 Mindlin-Reissner discontinuous plate model vs. FEA under differential actuation loading (i.e. equal moment magnitude but opposite directions). Solid lines correspond to analytical result, whereas circle markers to FEA.

E. Numerical Efficiency

This subsection summarises the presented work by evaluating the total percentage errors of the Mindlin-Reissner model—with respect to FEA—and by estimating the total number of degrees of freedom (DOFs) that each approach requires. Table 5 shows a summary of these degrees of freedom (DOFs) required for convergence. Furthermore, it shows the maximum RMS percentage error that both analytical models have, with respect to FEA. It can be observed that the number of DOFs increases by 66% when transverse shear is modeled, however, the analytical approach still needs only a very small fraction (around 1%) of the DOFs' that finite element

Table 5 Efficiency study, in terms of required degrees of freedom (DOFs) for convergence.

Model	DOFs	RMS Error [%]
FEA	1,086,426	–
Kirchhoff-Love	6,000	35.42
Mindlin-Reissner	10,000	9.13

analysis requires. In terms of CPU time, the Mindlin-Reissner discontinuous plate model is also more efficient as it takes on average 128.94 s to converge (when using 5 polynomial terms), whereas the FEM model takes on average 230.70 s (i.e. a 78.9% increase).

Furthermore, a summary of the comparison study between the Mindlin-Reissner discontinuous plate model and FEA is presented in Table 6. It can be observed that the maximum RMS error occurs when a single actuation input is applied. This maximum percentage error of $\approx 9\%$ is a significant improvement from the errors between 35% and 45% obtained using a Kirchhoff-Love discontinuous plate model [21].

VI. Experimental Validation: Static Displacement Measurements

To validate both the discontinuous Mindlin-Reissner analysis and the FEA Model, a series of experimental displacement measurements were performed on the composite FishBAC wind tunnel model under actuation loads. Displacements were measured at several chordwise and spanwise points using an Imetrum®3D Precision Displacement Tracker. The system consists of two-5 megapixel cameras in a stereo configuration, measuring at a 117 Hz frequency rate. These two cameras are mounted to a 3D measurement head (ICA-3D-0500-03) —a pre-calibrated frame where both cameras are installed at a fixed angle and distance from each other (Fig. 15). For the selected 3D measurement head, a measurement area of 600 mm $\times$ 600 mm with a 14 µm resolution is achieved [45].

Table 6 Maximum RMS error of Mindlin-Reissner discontinuous plate model, under different load cases. Errors are calculated with respect to Finite Element Analysis.

Load Case	RMS Error [%]	Maximum Error[%]
Symmetric	7.485	12.94
Single-Input	9.132	13.70
Differential	2.128	3.28

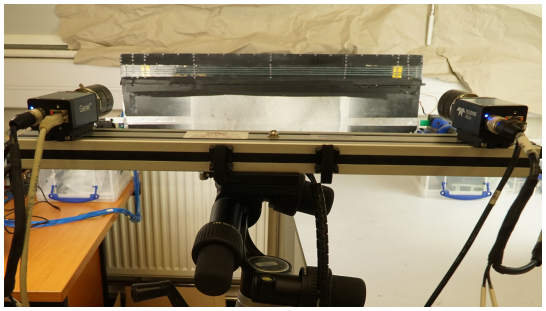

Fig. 15 Imetrum's 3D Precision Displacement Tracker system for in-plane and out-of-plane displacement measurements.

The actuation torque inputs can be estimated by measuring current in each actuator, and then using the DC motor's torque-current linear relationship [46]

$$T = \epsilon k_t I \,, \tag{12}$$

where ϵ is the mechanical efficiency factor of the actuation mechanism and k_t is the torque constant —which links the mechanical torque and current. The torque constant depends on the servo's magnetic circuit design and coil winding and can be calculated experimentally by performing a torque-current test. The torque constant of the KST X10 servos was obtained from a previous torque cell test [24], and it has an estimated value of $k_t = 0.82\,\mathrm{N\,A^{-1}}$—for a constant voltage of 6 V, used throughout the experiment. Furthermore, the mechanical efficiency factor ϵ was obtained experimentally by comparing analytical vs. experimental displacements. This efficiency factor accounts for frictional losses and energy loss due to tendon-pulley slack, friction at each pulley, energy loss due to deformation at the tendons, etc. During this experiment, the servos were controlled by prescribing Pulse-Width Modulation (PWM) signals using a *SSC-32U* control board.

To measure current, four (one per actuator) LEM® 6 A CASR 6-NP Hall Effect current sensors (Fig. 16) are used. These sensors measure the strength of the magnetic field induced by the current flow through the the actuator leads and generate an output voltage that is directly proportional to the magnitude of current—at a rate of $312.6\,\mathrm{mA\,V^{-1}}$. A series of 5 mm diameter bullseye stickers were used as target points, and voltage and current measurements were recorded using a National Instruments® USB-6211 data acquisition card. These tracking points were placed every 50 mm along the span at the trailing edge, as well as every 10 mm along the chord at the following locations: mid-span, three-quarter-span, chordwise free edge and at the center of the tendon. Three-dimensional position and displacements of each point were directly obtained from the point tracking software, and time averages are calculated at each point. These displacements are calculated based on the motion of each tracking point—around its surrounding pixels—relative to the previous frame. The presence of outliers was determined based on shape continuity, and were later removed from each data set.

A. Experimental Results

As explained in Section VI, the first step of the experimental validation is to estimate the efficiency factor ϵ of the actuation mechanism. A comparison between the analytical and experimental tip deflections was performed, and the efficiency factor is calculated using a linear fit. As observed in Fig. 17, the estimated mechanical efficiency factor is $\epsilon = 0.503$.

After estimating the efficiency factors, direct displacement comparisons can be established. First, the displacements along the

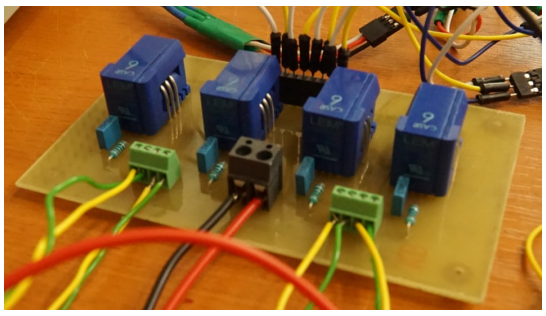

Fig. 16 Hall Effect actuator current sensor for estimating torque measurements

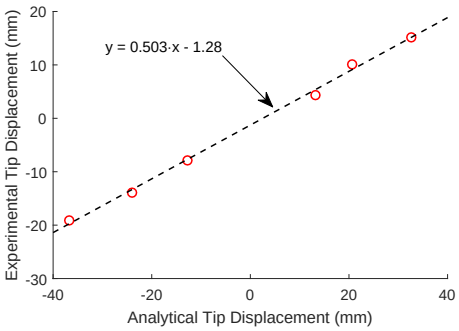

Fig. 17 Experimental vs. analytical tip deflection. Results are used to estimate the actuation mechanism efficiency factor.

spanwise edge are compared, as seen in Fig. 18. Note that, due to a reduced measuring area of 600 mm $\times$ 600 mm, only half of the span can be measured. Two different load cases are considered: positive (i.e. trailing edge up) and negative (i.e. trailing edge down) actuation. It is observed that the model predicts the downward displacements with an average error along the spanwise edge of 6.60% among the three downward deflections seen in Fig. 18. The upward trailing edge deflections are not predicted as well, as the average percentage error along the spanwise edge increases to 11.95% among the considered deflections. There appears to be an offset and the model overpredicts slightly the displacements, possibly due to glare and light reflections off of the silicone skin which, compounded by resolution and focus issues, did make point tracking more difficult for the positive displacements (i.e. away from the cameras). Furthermore, the transverse displacements was also tracked along the chordwise direction—at two spanwise locations. Fig. 19 shows transverse displacements along the chord, at midspan (left) and three-quarter-span (right). These results are consistent with those observed in Fig. 18: over-predicted positive deflections at mid-span, and good agreement at three-quarter-span.

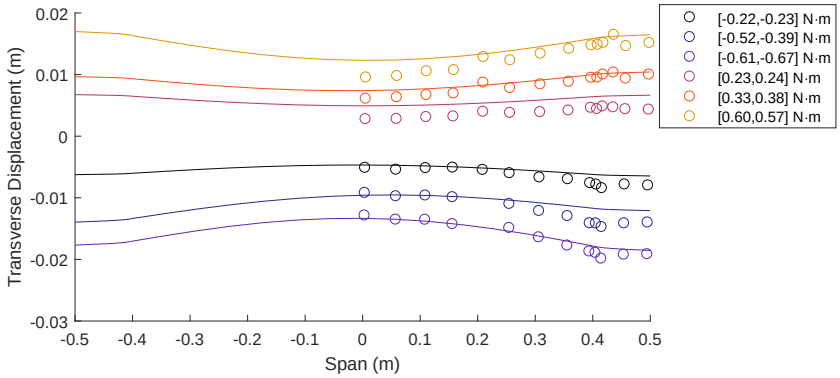

Fig. 18 Experimental (circle) vs. analytical(solid) tip deflection along the FishBAC's spanwise edge. Results are used to estimate the actuation mechanism efficiency factor

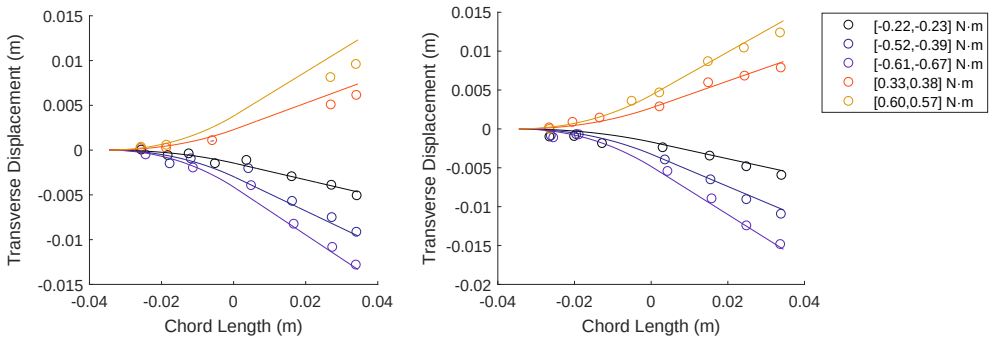

Fig. 19 Experimental (circle) vs. analytical (solid) transverse deflection, along chordwise direction, at two spanwise locations: mid-span (left) and three-quarter-span (right)

VII. Conclusion

A discontinuous, mesh-independent Mindlin-Reissner plate model was developed to model the highly anisotropic composite FishBAC morphing device. The novelty of this model lies in its ability to fully capture both chordwise and spanwise transverse shear displacements of the FishBAC—when subjected to different load cases—using only around 1% of the degrees of freedom of Finite Element Analysis. This model addresses the limitations of a previously developed Kirchhoff-Love plate model, which failed to predict the FishBAC's behavior at certain important load cases due to its inability to account for transverse shear strains.

Some of the main advantages of this model is that it converges on a fixed number of degrees of freedom, it does not require meshing and all the polynomial integrals can be calculated once up-front. These up-front polynomial integrations are performed and saved before the structural model is executed. Once the model is run, the required integrals are simply retrieved from a lookup table, meaning that all the computationally expensive steps are performed in advance. A summary of the main findings of this study is given as follows:

1) The Mindlin-Reissner plate theory-based model is able to predict the out-of-plane displacement of the FishBAC when the structure is subject to twist, with a percentage error of $\approx 2\%$ when compared to FEA.
2) The worst-case RMS error between the Mindlin-Reissner plate model and the numerical (FEA) solution for all of the loading conditions considered is approximately 9%, with typical RMS error values of 2-7%.
3) The Mindlin-Reissner plate model converges using 99% fewer Degrees of Freedom (DOFs) than the Finite Element Analysis approach. It is mesh-independent, parametrically defined, computationally efficient and can be used to model any continuous or discontinuous anisotropic plate structure subject to changes in thickness along either of the in-plane dimensions.
4) Average percentage differences of 6.60% (downward deflections) and 11.95% (upward deflections) were obtained when validating the discontinuous Mindlin-Reissner plate model against experimental results.

Future work using this model will include further design refinement and optimization of the FishBAC, as well as fluid-structure interaction analysis of this promising camber morphing composite device to fully capture its coupled aeroelastic behavior.

Acknowledgments

This work was supported by the Engineering and Physical Sciences Research Council through the EPSRC Centre for Doctoral

Training in Advanced Composites for Innovation and Science [grant number EP/L016028/1].

Furthermore, this project has received funding from the European Union's Horizon 2020 research and innovation programme under grant agreement No. 723491.

Data Access Statement

All underlying raw data used in this study are available for download from the Research Data Repository of University of Bristol, data.bris, at: https://doi.org/10.5523/bris.2bh76gwezip482na9b6fiemzci

References

[1] Barbarino, S., Bilgen, O., Ajaj, R. M., Friswell, M. I., and Inman, D. J., "A Review of Morphing Aircraft," *Journal of Intelligent Material Systems and Structures*, Vol. 22, No. 9, 2011, pp. 823–877. doi:10.1177/1045389X11414084.

[2] Woods, B. K. S., Bilgen, O., and Friswell, M. I., "Wind tunnel testing of the fish bone active camber morphing concept," *Journal of Intelligent Material Systems and Structures*, Vol. 25, No. 7, 2014, pp. 772–785. doi:10.1177/1045389X14521700.

[3] Sofla, A., Meguid, S., Tan, K., and Yeo, W., "Shape morphing of aircraft wing: Status and challenges," *Materials & Design*, Vol. 31, No. 3, 2010, pp. 1284–1292. doi:10.1016/j.matdes.2009.09.011, URL http://linkinghub.elsevier.com/retrieve/pii/S0261306909004968.

[4] Beaverstock, C., Woods, B., Fincham, J., and Friswell, M., "Performance Comparison between Optimised Camber and Span for a Morphing Wing," *Aerospace*, Vol. 2, No. 3, 2015, pp. 524–554. doi:10.3390/aerospace2030524, URL http://www.mdpi.com/2226-4310/2/3/524/.

[5] Parker, H., "The Parker Variable Camber," Tech. Rep. 77, National Advisory Committee for Aeronautics, Washington, DC, 1920.

[6] Hogan, H. J., "Variable Camber Airfoil," *U.S. Patent 1 ,868,748*, 1932.

[7] Chilton, R., "Variable Area-and-Camber Wing," *U.S. Patent 2,222,935*, 1940.

[8] Bilgen, O., Friswell, M. I., Kochersberger, K. B., and Inman, D. J., "Surface Actuated Variable-Camber and Variable-Twist Morphing Wings Using Piezocomposites," *Structures, Structural Dynamics and Materials Conference*, Vol. 19, No. April, 2011, pp. 1–13. doi:10.2514/6.2011-2072.

[9] Kota, S., Hetrick, J. A., Osborn, R., Paul, D., Pendleton, E., Flick, P., and Tilmann, C., "Design and application of compliant mechanisms for morphing aircraft structures," *Proc. SPIE*, Vol. 5054, No. November, 2003, pp. 24–33. doi:10.1117/12.483869, URL http://dx.doi.org/10.1117/12.483869.

[10] Barbarino, S., Pecora, R., Lecce, L., Concilio, A., Ameduri, S., and Calvi, E., "A novel SMA-based concept for airfoil structural morphing," *Journal of Materials Engineering and Performance*, Vol. 18, No. 5-6, 2009, pp. 696–705. doi:10.1007/s11665-009-9356-3.

[11] Diaconu, C. G., Weaver, P. M., and Mattioni, F., "Concepts for morphing airfoil sections using bi-stable laminated composite structures," *Thin-Walled Structures*, Vol. 46, No. 6, 2008, pp. 689–701. doi:10.1016/j.tws.2007.11.002.

[12] Daynes, S., Nall, S., Weaver, P., Potter, K., Margaris, P., and Mellor, P., "Bistable Composite Flap for an Airfoil," *Journal of Aircraft*, Vol. 47, No. 1, 2010, pp. 334–338. doi:10.2514/6.2009-2103, URL http://arc.aiaa.org/doi/abs/10.2514/6.2009-2103.

[13] Ai, Q., Azarpeyvand, M., Lachenal, X., and Weaver, P. M., "Aerodynamic and aeroacoustic performance of airfoils with morphing structures," *Wind Energy*, Vol. 19, No. 7, 2016, pp. 1325–1339. doi:10.1002/we.

[14] De Gaspari, A., and Ricci, S., "A Two Levels Approach for the Optimal Design of Morphing Airfoils," *13th AIAA/ISSMO Multidisciplinary Analysis Optimization Conference*, Vol. 9388, No. 13 - 15 September 2010, Fort Worth, Texas, 2010. doi:10.2514/6.2010-9388.

[15] Vasista, S., Riemenschneider, J., van de Kamp, B., Monner, H. P., Cheung, R. C. M., Wales, C., and Cooper, J. E., "Evaluation of a Compliant Droop-Nose Morphing Wing Tip via Experimental Tests," *Journal of Aircraft*, Vol. 54, No. 2, 2017, pp. 519–534. doi:10.2514/1.C033909, URL https://arc.aiaa.org/doi/10.2514/1.C033909.

[16] Larson, R. R., "Flight Control System Development and Flight Test Experience With the F-111 Mission Adaptive Wing Aircraft," Tech. rep., NASA Ames Research Center, Edwards, California, 1986.

[17] Kudva, J. N., "Overview of the DARPA Smart Wing Project," *Journal of Intelligent Materials Systems and Structures*, Vol. 15, No. 4, 2004, pp. 261–267. doi:10.1177/1045389X04042796.

[18] Campanile, L. F., and Sachau, D., "Belt-rib concept: a structronic approach to variable camber," *Journal of Intelligent Material Systems and Structures*, Vol. 11, No. 3, 2000, pp. 215–224. doi:10.1106/6H4B-HBW3-VDJ8-NB8A.

[19] Woods, B. K. S., and Friswell, M. I., "Preliminary Investigation of a Fishbone Active Camber Concept," *ASME Conference on Smart Materials, Adaptive Structures and Intelligent Systems*, 2012. doi:10.1017/CBO9781107415324.004.

[20] Rivero, A. E., Weaver, P. M., Cooper, J. E., and Woods, B. K., "Progress on the Design , Analysis and Experimental Testing of a Composite Fish Bone Active Camber Morphing Wing," *ICAST 2017: 28th International Conference on Adaptive Structures and Technologies*, Cracow, Poland, 2017, pp. 1–11.

[21] Rivero, A. E., Weaver, P. M., Cooper, J. E., and Woods, B. K., "Parametric structural modelling of fish bone active camber morphing aerofoils," *Journal of Intelligent Material Systems and Structures*, 2018, p. 1045389X1875818. doi:10.1177/1045389X18758182, URL http://journals.sagepub.com/doi/10.1177/1045389X18758182.

[22] Rivero, A. E., Weaver, P., and Woods, B. K., "Structural Modelling of Compliance-Based Morphing Structures under Transverse Shear Loading," *AIAA SciTech 2019 Forum*, American Institute of Aeronautics and Astronautics, San Diego, CA, 2019. doi:10.2514/6.2019-0229, URL https://arc.aiaa.org/doi/10.2514/6.2019-0229.

[23] Coburn, B. H., Wu, Z., and Weaver, P. M., "Buckling analysis of stiffened variable angle tow panels," *Composite Structures*, Vol. 111, No. 1, 2014, pp. 259–270. doi:10.1016/j.compstruct.2013.12.029, URL http://dx.doi.org/10.1016/j.compstruct.2013.12.029.

[24] Rivero, A. E., Fournier, S., Weaver, P. M., Cooper, J. E., and Woods, B. K. S., "Manufacturing and characterisation of a composite FishBAC morphing wind tunnel model," *ICAST 2018: 29th International Conference on Adaptive Structures and Technologies*, Seoul, Republic of Korea, 2018, pp. 1–14.

[25] Whitney, J. M., *Structural Analysis of Laminated Anisotropic Plates*, Technomic Publishing, Lancaster, Pennsylvania, 1987.

[26] Ilanko, S., Monterrubio, L., and Mochida, Y., *The Rayleigh-Ritz Method for Structural Analysis*, Iste Series, Wiley, London and New York, 2015.

[27] Livne, E., "Equivalent Plate Structural Modeling for Wing Shape Optimization Including Transverse Shear," *AIAA Journal*, Vol. 32, No. 6, 1994, pp. 1278–1288. doi:10.2514/3.12130.

[28] Giles, G. L., "Equivalent Plate Modeling for Conceptual Design of Aircraft Wing Structures," *1st AIAA Aircraft Engineering, Technology and Operations Congress*, Los Angeles, CA, 1995, pp. 1–17.

[29] Kim, E.-H., Roh, J.-H., Yoo, S.-J., and Lee, I., "Equivalent Plate Modeling of the Wing-Box Structure with Control Surface," *KSAS International Journal*, Vol. 7, No. 2, 2006, pp. 104–109. doi:10.5139/IJASS.2006.7.2.104.

[30] Yang, Y., Wu, Z., and Yang, C., "Equivalent Plate Modeling for Complex Wing Configurations," *Procedia Engineering*, Vol. 31, 2012, pp. 409–415. doi:10.1016/j.proeng.2012.01.1044, URL http://dx.doi.org/10.1016/j.proeng.2012.01.1044.

[31] Timoshenko, S. P., "LXVI. On the correction for shear of the differential equation for transverse vibrations of prismatic bars," *Philosophical Magazine Series 6*, Vol. 41, No. 245, 1921, pp. 744–746. doi:10.1080/14786442108636264.

[32] Oñate, E., *Thick/Thin Plates. Reissner-Mindlin Theory*, Springer Netherlands, Dordrecht, 2013. doi:10.1007/978-1-4020-8743-1{_}6, URL https://doi.org/10.1007/978-1-4020-8743-1_6.

[33] Coburn, B. H., "Buckling of stiffened variable stiffness panels," Ph.D. thesis, University of Bristol, 2015.

[34] Hyer, M. H., *Stress Analysis of Fiber-Reinforced Composite Materials*, McGraw-Hill, New Delhi, 2014.

[35] Jaunky, N., Knight, N., and Ambur, D., "Buckling of arbitrary quadrilateral anisotropic plates," *AIAA Journal*, Vol. 33, No. 5, 1995, pp. 938–944. doi:10.2514/3.12512, URL http://dx.doi.org/10.2514/3.12512.

[36] Groh, R. M., and Weaver, P. M., "Static inconsistencies in certain axiomatic higher-order shear deformation theories for beams, plates and shells," *Composite Structures*, Vol. 120, 2015, pp. 231–245. doi:10.1016/j.compstruct.2014.10.006, URL http://dx.doi.org/10.1016/j.compstruct.2014.10.006.

[37] Vescovini, R., and Bisagni, C., "Buckling analysis and optimization of stiffened composite flat and curved panels," *AIAA Journal*, Vol. 50, No. 4, 2012, pp. 904–915. doi:10.2514/1.J051356.

[38] Wu, Z., Raju, G., and Weaver, P. M., "Framework for the Buckling Optimization of Variable-Angle Tow Composite Plates," *AIAA Journal*, Vol. 53, No. 12, 2015, pp. 3788–3804. doi:10.2514/1.J054029, URL http://arc.aiaa.org/doi/abs/10.2514/1.J054029.

[39] KST, "X10 Wing Servo," , 2017. URL https://www.hyperflight.co.uk/getfile.asp?code=KST-X10&code2=1.

[40] D3039, "Standard Test Method for Tensile Properties of Polymer Matrix Composite Materials," *ASTM International*, Vol. 08, 2014, pp. 1–13. doi:10.1520/D3039.

[41] D3518, "Standard Test Method for In-Plane Shear Response of Polymer Matrix Composite Materials by Tensile Test," *ASTM International*, Vol. 94, No. Reapproved, 2007, pp. 1–7. doi:10.1520/D3518.

[42] D638, "Standard test method for tensile properties of plastics," *ASTM International*, 2013, pp. 1–16. doi:10.1520/D0638-10.1.

[43] Cline, A. K., Moler, C. B., Stewart, G. W., and Wilkinson, J. H., "An Estimate for the Condition Number of a Matrix," *SIAM Journal on Applied Mathematics*, Vol. 16, No. 2, 1979, pp. 368–375.

[44] Groh, R. M., "Non-classical effects in straight-fibre and tow-steered composite beams and plates," Ph.D. thesis, University of Bristol, 2015.

[45] Imetrum, "3D Measurement Head Range," , 2018.

[46] Maxon, "maxon DC motor and maxon EC motor," , 2014.